Journal of Sound and Vibration 329 (2010) 2367–2383

Contents lists available at ScienceDirect

Journal of Sound and Vibration

journal homepage: www.elsevier.com/locate/jsvi

A local flexibility method for vibration-based damage localization and quantification

Edwin Reynders *, Guido De Roeck

Katholieke Universiteit Leuven, Department of Civil Engineering, Kasteelpark Arenberg 40, B-3001 Leuven, Belgium

ARTICLE INFO

Article history:
Accepted 19 April 2009
The peer review of this article was organised by the Guest Editor.
Available online 3 June 2009

ABSTRACT

A method for vibration-based damage localization and quantification, based on quasi-static flexibility, is presented. The experimentally determined flexibility matrix is combined with a virtual load that causes nonzero stresses in a small part of the structure, where a possible local stiffness change is investigated. It is shown that, if the strain–stress relationship for the load is proportional, the ratio of some combination of deformations before and after a stiffness change has occurred, equals the inverse local stiffness ratio. The method is therefore called local flexibility (LF) method. Since the quasi-static flexibility matrix can be composed directly from modal parameters, the LF method allows to determine local stiffness variations directly from measured modal parameters, even if they are determined from output-only data. Although the LF method is in principle generally applicable, the emphasis in this paper is on beam structures. The method is validated with simulation examples of damaged isostatic and hyper-static beams, and experiments involving a reinforced concrete free–free beam and a three-span prestressed concrete bridge, that are both subjected to a progressive damage test.

1. Introduction

Vibration-based damage identification methods have some specific advantages over other methods that are used for structural damage identification: they are nondestructive and they are able to identify damage that is invisible at the surface. Moreover, they are 'global' because no a priori location of the damage has to be assumed as opposed to local methods such as ultrasonic testing. The fact that for some of these vibration-based damage identification methods no artificial excitation is needed, but only the response at certain degrees of freedom (DOFs) of the structure, is another important advantage because the structure can remain in operation. As a consequence, these methods can be used for permanent health monitoring. A disadvantage is that factors other than damage like for instance temperature also influence the structure's dynamic parameters, in particular the eigenfrequencies, which makes that these environmental influences often need to be taken into account [24,25]. Vibration-based methods have been applied successfully on large and complicated structures such as civil engineering structures (mostly bridges and offshore platforms), aerospace structures and composite structures.

During the last decades, research on vibration-based structural damage identification methods has been expanding rapidly, as evidenced by a profound literature review covering practically all methods up to 1996 [7] and an extensive update which covers the new developments published between 1996 and 2001 [30]. Vibration-based damage

* Corresponding author.
E-mail addresses: edwin.reynders@bwk.kuleuven.be (E. Reynders), guido.deroeck@bwk.kuleuven.be (G. De Roeck).

0022-460X/$ - see front matter © 2009 Elsevier Ltd. All rights reserved.
doi:10.1016/j.jsv.2009.04.026

identification is classified into four levels [28]: (1) damage detection, (2) damage localization, (3) damage quantification and (4) prediction of the remaining service-life of the structure.

Two main types of vibration-based damage identification techniques can be discriminated: model based and non model based, also called parametric and nonparametric, respectively [2]. Parametric methods are based on a model of the structure, some parameters of which are adjusted using vibration measurements, by minimizing the difference between the modal parameters computed with the model and the ones that are derived from the measurements. This optimization problem is often nonconvex, which makes that the real optimum might be missed, resulting in wrong parameter values. Global iterative optimization methods exist to solve this problem, such as coupled local minimizers [33], genetic algorithms [11], or simulated annealing [13]. In addition, the performance of parametric methods depends on the accuracy of the model and on the selected damage parameters, and the results might be very sensitive to the measured modal parameters, since a local optimum might become the global optimum and vice versa. As a result, the obtained parameters are consistent with the measured modal data, but they may be unrelated to their true values. An example of a parametric damage identification method is finite element model updating (FEMU) [19], which has shown to be capable of in situ damage identification of levels 1–3, as illustrated in Refs. [27,32].

Nonparametric methods do not need a detailed model of the structure and as a consequence do not suffer from the related difficulties. Most of the existing nonparametric damage identification methods that involve damage localization and/or quantification are based on changes in mode shapes [36,37,9,29], mode shape curvatures [22,15], or dynamically measured flexibilities [20,21,3]. This paper focuses on dynamically measured flexibilities. The flexibility matrix equals the inverse of the stiffness matrix of a structure and therefore Aktan et al. define *damage* as a measurable increase in the incremental local flexibility (LF) of a critical region [1]. The use of flexibility instead of stiffness is motivated by the fact that the dynamically measured flexibility matrix is dominated by the lowest modes of a structure, which can be easily measured, while the dynamically measured stiffness matrix is dominated by the highest modes of the structure, which are hard if not impossible to measure [20]. If changes in environmental conditions (temperature, boundary conditions, etc.) of a structure cause a significant stiffness reduction, they can be interpreted as damage, in consistency with the above definition. However, one should keep in mind that sometimes an important stiffness variation does not correspond to physical damage. For instance when a structure contains a thick asphalt layer and the temperature drops under 0 °C, the stiffness can increase significantly, and vice versa when the temperature rises above 0 °C [25,35]. Therefore, it is important to compare the derived local flexibilities with values that define a 'safe' state of the structure, such as baseline measurements or design values.

Pandey and Biswas [20,21] propose to use the column-wise maximum absolute difference of flexibility matrices as an indicator for damage localization. Simulated and measured flexibilities for steel beams with different support conditions illustrate that an ad hoc interpretation of this indicator is necessary for different types of structures and different types of boundary conditions. Toksoy and Aktan [34] used dynamically measured flexibilities for damage localization of a reinforced concrete bridge which is subject to progressive damage tests. They observe that flexibility is a very sensitive damage indicator as opposed to eigenfrequencies and damping ratios. By comparing the deflections obtained from a combination of a measured flexibility matrix with a uniform load and a line load before and after a damage test, damage localization was successful. Aktan et al. [1] find a very good match between the measured deflection of a steel stringer bridge under truck loading and the corresponding deflection calculated using dynamically measured flexibility. Furthermore, damage localization on a steel truss highway bridge that was subjected to a progressive damage test by comparing the combination of the dynamically measured flexibility with a uniform load and a point load, was reported to be successful. Mayes [18] proposes to use measured flexibility multiplied by a unit load at the position where an artificial force was applied for a modal test as the input for a damage identification method called STRETCH. Applying this method to detect and locate progressively induced damage on a three-span bridge, localization turned out to be possible only for large amounts of damage. Zhang and Aktan [38] suggest that the curvature of the 'uniform load surface', i.e. measured flexibility combined with a uniformly distributed load, is a highly sensitive damage indicator. It is confirmed by simulation of flexibility measurements using a three-span numerical bridge model.

The theoretical relationship between these damage indicators and the definition of damage provided above is not clear, however. A flexibility-based damage identification method that has a solid theoretical and physical base is the damage locating vector technique of Bernal [4]. He showed that if a load configuration exists for which the displacements before and after damage occurred are the same, the stresses caused by the loading are zero in the damaged zones. As a result, by finding a base for the null space of the difference in flexibility matrix, damage localization is possible. The technique has been recently extended towards output-only measurements [5].

The calculation of *local* flexibilities, in accordance with the definition of damage by Aktan et al. [1] given above, has been an open problem for quite sometime. An illustration of this is that the proposed damage indicators given above are useful for damage detection and localization (level 2 damage identification), but not for damage quantification (level 3), at least not on a solid physical basis. In this paper, a local flexibility (LF) method is presented that makes use of the dynamic flexibility matrix, also called receptance matrix or force–displacement FRF (frequency response function) matrix, that is evaluated at zero frequency to yield the quasi-static flexibility matrix. Combining the quasi-static flexibility matrix with a virtual load that causes stresses in the vicinity of one measurement location only yields a virtual quasi-static deformation. From the principle of virtual work, it is shown that, if the strain–stress relationship for the given load is proportional, the

ratio of some linear combination of displacements before and after a change in stiffness has occurred, equals the inverse local stiffness ratio. As a result, the LF method permits not only a localization of these changes (level 2 damage identification), but also a quantification (level 3 damage identification). Note that the LF method does not require that any force configuration is actually applied to the structure: the *measured* flexibility matrix is multiplied with a *virtual* force vector. Although the LF method is in principle applicable to any structural type, the emphasis in this paper is on beam structures.

The organization of the text is as follows. The theoretical basis of the LF method is treated in Section 2. In Section 3, the application to the estimation of the bending stiffness reduction of beam structures is discussed. How to obtain flexibility matrices from forced and ambient vibration tests is indicated in Section 4. The method is illustrated in Section 5 with simulations of an isostatic beam with asymmetric damage and a hyperstatic beam with multiple damage locations. In Section 6, the application of the LF method for damage localization and quantification on a progressively damaged reinforced concrete beam with multiple damage locations is presented. The application of the method on a progressively damaged three-span reinforced concrete bridge is treated in detail in Section 7. The paper ends with the conclusions drawn from the simulations and experiments.

2. Theoretical basis of the local flexibility method

2.1. General principle

Consider a structure with volume Ω and boundary Γ that is subject to Dirichlet boundary conditions $\boldsymbol{u} = \bar{\boldsymbol{u}}$ along part of the boundary (Fig. 1). A first load system, composed of some linear combination $\boldsymbol{f^1} = \sum_{k_i=1}^{l} w_{k_i}^1 \boldsymbol{f_{k_i}^1}$ of forces $\boldsymbol{f_{k_i}^1}$, is applied to the structure. The forces $\boldsymbol{f_{k_i}^1}$ are applied at a limited number of l degrees of freedom (DOFs) k_i, where k stands for a particular point and i for a particular direction. The collection of l DOFs should be thought of as DOFs that can be measured with a static or dynamic test. The load system is chosen such that the induced stress field $\boldsymbol{\sigma^1}$ (i) can be calculated from the loading only (i.e., without knowledge of the structure's stiffness) and (ii) consists of nonzero stresses in a small volume Ω_k only. The only assumption that is made is that the stiffness within Ω_k is constant.

Consider the same structure as in Fig. 1, subjected to a second load system composed of some other linear combination $\boldsymbol{f^2} = \sum_{k_i=1}^{l} w_{k_i}^2 \boldsymbol{f_{k_i}^2}$ of forces $\boldsymbol{f_{k_i}^2}$ at the considered DOFs k_i.

The virtual work principle states that

$$\int_{\Omega} \rho \boldsymbol{b}^T \delta \boldsymbol{u} \, \mathrm{d}\Omega + \int_{\Gamma} \boldsymbol{t}^T \delta \boldsymbol{u} \, \mathrm{d}\Gamma = \int_{\Omega} \boldsymbol{\sigma}^T \delta \boldsymbol{\varepsilon} \, \mathrm{d}\Omega, \tag{1}$$

where $\boldsymbol{b} \in \mathbb{R}^{3\times 1}$ is the vector with body forces, $\boldsymbol{t} \in \mathbb{R}^{3\times 1}$ the vector with applied tractions, $\boldsymbol{\sigma} \in \mathbb{R}^{6\times 1}$ the corresponding stress vector, $\delta \boldsymbol{u} \in \mathbb{R}^{3\times 1}$ a virtual displacement field that obeys the Dirichlet boundary conditions and $\delta \boldsymbol{\varepsilon} \in \mathbb{R}^{6\times 1}$ the corresponding virtual strain vector. If the virtual displacement field is chosen as the one that is created by load system 1 (the forces $\boldsymbol{f^1}$) and the forces and the stresses are due to the second load system (the forces $\boldsymbol{f^2}$), one has that

$$\sum_{k_i=1}^{l} w_{k_i}^2 f_{k_i}^2 u_{k_i}^1 = \int_{\Omega_k} \boldsymbol{\sigma^2}^T \boldsymbol{\varepsilon^1} \, \mathrm{d}\Omega_k, \tag{2}$$

where $u_{k_i}^1$ is the displacement at DOF k_i corresponding to a force at that DOF. This shows that $\boldsymbol{u^1}$ is only dependent on the (possibly nonlinear) stress–strain relationship *inside* Ω_k.

Suppose that the structure is linear elastic and that $\boldsymbol{\sigma^1}$ is chosen such that $\boldsymbol{\varepsilon^1}$ is proportional to $\boldsymbol{\sigma^1}$ with stiffness constant $1/K$. This means that for an isotropic structure where K equals the modulus of elasticity E, $\boldsymbol{\sigma^1}$ can be chosen

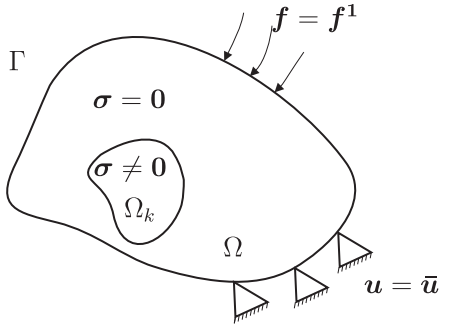

Fig. 1. Structure subjected to forces $\boldsymbol{f^1}$ that cause nonzero stresses in Ω_k only.

arbitrarily as long as Poisson's ratio can be considered as constant since

$$\begin{bmatrix} \varepsilon_{xx} \\ \varepsilon_{yy} \\ \varepsilon_{zz} \\ \varepsilon_{xy} \\ \varepsilon_{yz} \\ \varepsilon_{zx} \end{bmatrix} = \frac{1}{E} \begin{bmatrix} 1 & -\nu & -\nu & 0 & 0 & 0 \\ -\nu & 1 & -\nu & 0 & 0 & 0 \\ -\nu & -\nu & 1 & 0 & 0 & 0 \\ 0 & 0 & 0 & 1+\nu & 0 & 0 \\ 0 & 0 & 0 & 0 & 1+\nu & 0 \\ 0 & 0 & 0 & 0 & 0 & 1+\nu \end{bmatrix} \begin{bmatrix} \sigma_{xx} \\ \sigma_{yy} \\ \sigma_{zz} \\ \sigma_{xy} \\ \sigma_{yz} \\ \sigma_{zx} \end{bmatrix}.$$

If $\sum_{k_i=1}^{L} w_{k_i}^2 f_{k_i}^2 u_{k_i}^1$ is calculated before ($u_{k_iU}^1$) and after damage has occurred ($u_{k_iD}^1$), one has

$$\frac{\sum_{k_i=1}^{L} w_{k_i}^2 f_{k_i}^2 u_{k_iU}^1}{\sum_{k_i=1}^{L} w_{k_i}^2 f_{k_i}^2 u_{k_iD}^1} = \frac{\int_{\Omega_k} \boldsymbol{\sigma}_{\mathbf{2}}^T \frac{\boldsymbol{\sigma}_{\mathbf{1}}}{K} \mathrm{d}\Omega_k}{\int_{\Omega_k} \boldsymbol{\sigma}_{\mathbf{2}}^T \frac{\boldsymbol{\sigma}_{\mathbf{1}}}{K+\Delta K} \mathrm{d}\Omega_k} = \frac{K+\Delta K}{K}, \tag{3}$$

where ΔK is the change in the stiffness parameter in Ω_k due to damage. It is assumed that ΔK is constant within Ω_k.

3. Application to the bending stiffness of beam structures

In this section, the general framework of Section 2 is elaborated for the estimation of changes of bending stiffness of isostatic and hyperstatic beams. This means that the stiffness parameter K of (3) is substituted by EI where E is the modulus of elasticity in section Ω_k and I is the moment of inertia in section Ω_k of the beam's cross-section with respect to the transversal axis.

Theorem 1. *If shear deformation can be neglected and EI is constant between equidistant points $k-2$ and $k+2$, the force configuration of Fig. 2 causes nonzero stresses between points $k-2$ and $k+2$ only. This is valid for isostatic and hyperstatic structures. In other words, if the structure of Fig. 1 is a beam and the Dirichlet boundary conditions $\boldsymbol{u} = \bar{\boldsymbol{u}}$ correspond to static or hyperstatic boundary conditions, Ω_k of Fig. 1 corresponds to the zone between $k-2$ and $k+2$ of Fig. 2 if $\boldsymbol{f}^{\mathbf{1}}$ of Fig. 1 corresponds to the force configuration of Fig. 2.*

Proof. For the theorem to hold, it is sufficient that

- the vector sum of all forces of Fig. 2 is zero;
- the resulting moment of all forces of Fig. 2 at any point is zero;
- the relative rotation between points $k-2$ and $k+2$, due to the force configuration, is zero.

Checking the first two conditions is trivial. The third condition can be checked by means of the virtual work principle. The load configuration of Fig. 2 is chosen as the virtual load configuration. It produces the bending moments shown in Fig. 3.

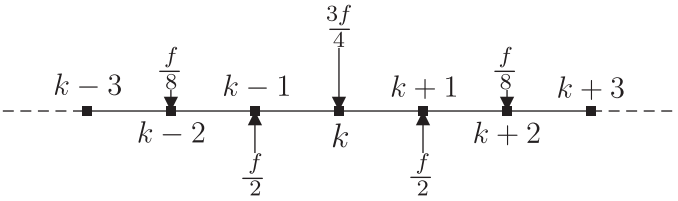

Fig. 2. Beam structure: load configuration $\boldsymbol{f}^{\mathbf{1}}$ that causes virtual stresses and strains around one particular measurement DOF k only.

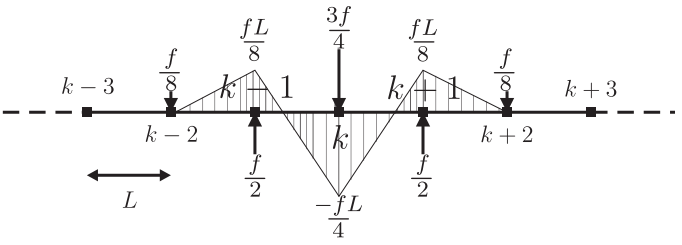

Fig. 3. Theorem 1: bending moments due to the load configuration of Fig. 2.

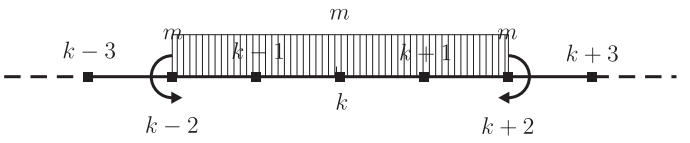

Fig. 4. Theorem 1: virtual force configuration and corresponding bending moments.

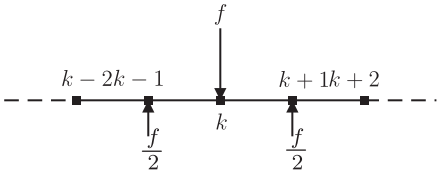

Fig. 5. Beam structure: possible second load configuration $\boldsymbol{f^2}$.

This is chosen as the virtual load configuration. The second, real load configuration consists of two bending moments of opposite sign, at nodes $k-2$ and $k+2$. The corresponding bending moments are shown in Fig. 4.

Application of the virtual work principle (1) yields, with the chosen real load configuration of Fig. 4 and virtual load configuration of Fig. 3:

$$\int_{\Gamma} \boldsymbol{t}^T \delta \boldsymbol{u}\, \mathrm{d}\Gamma = \int_{\Omega} \boldsymbol{\sigma}^T \delta \boldsymbol{\varepsilon}\, \mathrm{d}\Omega$$

$$m\varphi_{k-2} - m\varphi_{k+2} = \int_{k-2}^{k+2} M^1(x)\frac{M^2(x)}{EI}\,\mathrm{d}x$$

$$= \int_{k-2}^{k+2} \cdot \frac{1}{EI} \cdot \mathrm{d}x$$

$$= 0,$$

where φ_{k-2} is the rotation at node $k-2$ and φ_{k+2} is the rotation at node $k+2$ when the load configuration of Fig. 2 is applied. The relative rotation between both nodes is zero, which shows that also the third condition holds. □

From Theorem 1, it is clear that the load configuration of Fig. 2 can be applied as the first load configuration $\boldsymbol{f^1}$ of Section 2, causing virtual displacements and strains. The second load configuration $\boldsymbol{f^2}$ can be any configuration that obeys the boundary conditions, like for instance the configuration of Fig. 5.

Under the basic assumptions of Theorem 1, one has from (2), where load configuration $\boldsymbol{f^1}$ is shown in Fig. 2 and load configuration $\boldsymbol{f^2}$ is shown in Fig. 5, that

$$\sum_{k_i=1}^{l} w_{k_i}^2 f_{k_i}^2 u_{k_i}^1 = \int_{\Omega_k} \boldsymbol{\sigma^2}^T \boldsymbol{\varepsilon^1}\, \mathrm{d}\Omega_k$$

$$u_k^1 - \frac{1}{2}(u_{k-1}^1 + u_{k+1}^1) = \int_{k-2}^{k+2} M^2(x)\frac{M^1(x)}{EI}\,\mathrm{d}x.$$

It then follows from (3) that

$$\frac{u_{kU}^1 - \frac{1}{2}(u_{k-1U}^1 + u_{k+1U}^1)}{u_{kD}^1 - \frac{1}{2}(u_{k-1D}^1 + u_{k+1D}^1)} = \frac{EI + \Delta EI}{EI}. \tag{4}$$

Other force configurations $\boldsymbol{f^2}$ lead to the following alternative formulae:

$$\frac{\sum_{k_i=1}^{l} w_{k_i} u_{k_iU}^1}{\sum_{k_i=1}^{l} w_{k_i} u_{k_iD}^1} = \frac{EI + \Delta EI}{EI} \quad \text{or} \quad \frac{\|\boldsymbol{u_U^1}\|_1}{\|\boldsymbol{u_D^1}\|_1} = \frac{EI + \Delta EI}{EI}, \tag{5}$$

where w_{k_i} are arbitrary weights and $\|\bullet\|_1$ stands for the 1-norm. The 1-norm is from the numerical point of view a good choice, since subtractions are avoided. However, it can only be used if the sign of the corresponding elements of $\boldsymbol{u}_{\boldsymbol{U}}^{\boldsymbol{1}}$ and $\boldsymbol{u}_{\boldsymbol{D}}^{\boldsymbol{1}}$ is the same.

Note 1. For isostatic beams, as an alternative to the force configuration $\boldsymbol{f}^{\boldsymbol{1}}$ of Fig. 2, the force configuration of Fig. 5 can be applied. The proof is trivial since for isostatic structures, it is not necessary that the relative rotation between points $k-1$ and $k+1$ be zero in order to have nonzero stresses between these points only.

4. Realization using measured flexibility

4.1. General principle

The dynamic flexibility matrix $\boldsymbol{H}(\omega)$, also called receptance matrix or force–displacement FRF matrix, between l measured DOFs of the structure, is defined from

$$\boldsymbol{u}(\omega) = \boldsymbol{H}(\omega)\boldsymbol{f}(\omega), \tag{6}$$

where ω is the circular frequency, $\boldsymbol{u}(\omega) \in \mathbb{C}^{l\times 1}$ is the vector with measured DOFs and $\boldsymbol{f}(\omega) \in \mathbb{C}^{l\times 1}$ is the vector with forces at the measured DOFs. If $\boldsymbol{H}(\omega)$ is evaluated at $\omega = 0$, it is only dependent on the structure's stiffness. Suppose $\boldsymbol{H}(0)$ is measured in the undamaged as well as in the damaged configuration, which is indicated as $\boldsymbol{H}_{\boldsymbol{U}}(0)$ and $\boldsymbol{H}_{\boldsymbol{D}}(0)$, respectively. As indicated in (6), the multiplication of $\boldsymbol{H}_{\boldsymbol{U}}(0)$ and $\boldsymbol{H}_{\boldsymbol{D}}(0)$ with a virtual force configuration $\boldsymbol{f}(0)$ that yields nonzero stresses at a small volume Ω_k of the structure only, equals the displacement vector $\boldsymbol{u}_{\boldsymbol{U}}(0)$ for the undamaged and $\boldsymbol{u}_{\boldsymbol{D}}(0)$ for the damaged configuration, respectively. The relative change of the stiffness parameter is then calculated from (3). Note that this approach does not require that any force configuration is actually applied to the structure: the *measured* flexibility matrix is multiplied with a *virtual* force vector.

In the specific case of beam structures, the measured flexibility matrices $\boldsymbol{H}_{\boldsymbol{U}}(0)$ and $\boldsymbol{H}_{\boldsymbol{D}}(0)$ are multiplied with the virtual force vector of Fig. 2 or 5, depending on whether the beam is hyperstatic or isostatic, respectively. From (6), it follows that the result of this multiplication equals a displacement vector: $\boldsymbol{u}_{\boldsymbol{U}}(0)$ for the undamaged and $\boldsymbol{u}_{\boldsymbol{D}}(0)$ for the damaged configuration. Eqs. (4) or (5) are then used to estimate the corresponding local stiffness change.

An estimate of $\boldsymbol{H}(0)$ can be obtained from forced or ambient vibration tests, as indicated in Sections 4.2 and 4.3, respectively. $\boldsymbol{H}(0)$ could be measured directly from a static load–deflection test as well. However, the estimation of $\boldsymbol{H}(0)$ from ambient vibrations has the important advantage that no artificial force needs to be applied to the structure. This makes the approach suitable for permanent structural health monitoring.

4.2. Obtaining quasi-static flexibilities from forced vibration tests

A classical result from experimental modal analysis of mechanical systems is the modal decomposition of the receptance matrix [8,10,17]:

$$\boldsymbol{H}(\omega) \approx \boldsymbol{H}^{\boldsymbol{m}}(\omega) = \sum_{k=1}^{n} \frac{q_k \boldsymbol{\phi}_{\boldsymbol{k}} \boldsymbol{\phi}_{\boldsymbol{k}}^{\mathrm{T}}}{i\omega - \lambda_k} + \frac{\overline{q_k}\,\overline{\boldsymbol{\phi}_{\boldsymbol{k}}}\,\boldsymbol{\phi}_{\boldsymbol{k}}^{*}}{i\omega - \overline{\lambda_k}}, \tag{7}$$

where λ_k is system pole corresponding to mode k, $\boldsymbol{\phi}_{\boldsymbol{k}}$ is the corresponding mode shape, and q_k the corresponding modal scaling factor. $\bar{\bullet}$ denotes complex conjugate, $\bullet^{\mathrm{T}}$ denotes transpose and $\bullet^{*}$ denotes conjugate transpose. Evaluation at $\omega = 0$ yields the quasi-static flexibility matrix. The approximation in (7) is due to the fact that the number of measured modes n is limited, i.e., a modal truncation takes place. However, since at $\omega = 0$ the denominator of (7) is only small for modes with an eigenfrequency $\omega_k \to 0$, only the modes corresponding to the lowest eigenfrequencies are needed for an accurate approximation of $\boldsymbol{H}(0)$. This is illustrated in the simulation examples of Section 5 and the applications of Sections 6 and 7.

4.3. Obtaining quasi-static flexibilities from ambient vibration tests

It is well known (see for instance [12]) that a dynamic linear mechanical structure can be described numerically with a state-space model:

$$\frac{\mathrm{d}\boldsymbol{x}(t)}{\mathrm{d}t} = \boldsymbol{A}_{\boldsymbol{c}} \cdot \boldsymbol{x}(t) + \boldsymbol{B}_{\boldsymbol{c}} \cdot \boldsymbol{f}(t), \quad \boldsymbol{x}(t) = \begin{bmatrix} \boldsymbol{u}(t) \\ \frac{\mathrm{d}\boldsymbol{u}(t)}{\mathrm{d}t} \end{bmatrix}, \tag{8}$$

where $\boldsymbol{u}(t)$ is the displacement vector and $\boldsymbol{f}(t)$ is the vector with applied forces. $\boldsymbol{x}(t)$ is called the state of the structure. In ambient vibration tests, some responses of the structure are measured. Suppose that they are grouped in a vector $\boldsymbol{y}(t)$. If the measured quantities are displacements or velocities, one has

$$\boldsymbol{y}(t) = \boldsymbol{C}_{\boldsymbol{d}}\boldsymbol{x}(t) \quad \text{or} \quad \boldsymbol{y}(t) = \boldsymbol{C}_{\boldsymbol{v}}\boldsymbol{x}(t), \tag{9}$$

respectively. In case of measured accelerations, one has

$$\boldsymbol{y}(t) = \boldsymbol{C_a x}(t) + \boldsymbol{D f}(t), \tag{10}$$

where $\boldsymbol{D}$ is the direct transmission term, which is only dependent on the mass of the structure.

From a simple Fourier transform of (8) and (9), one has the following expression for the receptance matrix:

$$\boldsymbol{H}(0) = -\boldsymbol{C_d A_c^{-1} B_c}. \tag{11}$$

From differentiation of the left equation of (9), it can be shown that [5]

$$\underbrace{\begin{bmatrix} \boldsymbol{C A_c^{b-1}} \\ \boldsymbol{C A_c^{b-2}} \end{bmatrix}}_{\boldsymbol{H_p}} \boldsymbol{B_c} = \underbrace{\begin{bmatrix} \boldsymbol{I} \\ \boldsymbol{0} \end{bmatrix}}_{\boldsymbol{L}} \boldsymbol{D},$$

where in case of displacement measurements $\boldsymbol{C} = \boldsymbol{C_d}$ and $b = 2$, in case of velocity measurements $\boldsymbol{C} = \boldsymbol{C_v}$ and $b = 1$ and in case of acceleration measurements $\boldsymbol{C} = \boldsymbol{C_a}$ and $b = 0$. Solving this equation for $\boldsymbol{B_c}$ in a least-squares sense and substituting the result in (11) yields

$$\boldsymbol{H}(0) = -\boldsymbol{C A_c^{b-3} H_p^{\dagger} L D}.$$

If $\boldsymbol{D}$ is diagonal, which is in almost all practical cases a good assumption, and if the structure's mass is approximately equally distributed, one has

$$\boldsymbol{H}(0) \approx -m \underbrace{\boldsymbol{C A_c^{b-3} H_p^{\dagger} L}}_{\boldsymbol{H_a^m}(0)}, \tag{12}$$

where m is an unknown mass-dependent constant. If the assumptions of lumped mass and equal mass distribution are not valid, the measured modes could be scaled using the analytical mass matrix and the approach of Section 4.2 could be used.

An eigenvalue decomposition of $\boldsymbol{A_c}$ leads to the state space model in modal coordinates:

$$\frac{\mathrm{d}\boldsymbol{x^m}(t)}{\mathrm{d}t} = \boldsymbol{\Lambda_c x^m}(t) + \boldsymbol{B_c^m f}(t),$$

$$\boldsymbol{y}(t) = \boldsymbol{\Phi x^m}(t) + \boldsymbol{D f}(t),$$

where

$$\boldsymbol{A_c} = \boldsymbol{\Psi \Lambda_c \Psi^{-1}}, \quad \boldsymbol{x^m}(t) = \boldsymbol{\Psi^{-1} x}(t), \quad \boldsymbol{B_c} = \boldsymbol{\Psi^{-1} B}, \quad \boldsymbol{\Phi} = \boldsymbol{C \Psi},$$

$$\boldsymbol{\Phi} = [\boldsymbol{\phi_1} \cdots \boldsymbol{\phi_n}\ \ \overline{\boldsymbol{\phi_1}} \cdots \overline{\boldsymbol{\phi_n}}] \quad \text{and} \quad \boldsymbol{\Lambda_c} = \mathrm{diag}([\boldsymbol{\lambda_1} \cdots \boldsymbol{\lambda_n}\ \ \overline{\boldsymbol{\lambda_1}} \cdots \overline{\boldsymbol{\lambda_n}}]).$$

$\boldsymbol{\Lambda_c}$ is a diagonal matrix containing the system poles. The columns of $\boldsymbol{\Phi}$ are the (unscaled) observed mode shapes. Considering the state space model in modal coordinates, $\boldsymbol{H_a^m}(0)$, (12) can be written as

$$\boldsymbol{H_a^m}(0) = -\boldsymbol{\Phi \Lambda_c^{-1}} (\boldsymbol{\Lambda_c^* \Phi^* \Phi \Lambda_c} + \boldsymbol{\Phi^* \Phi}) \boldsymbol{\Lambda_c^* \Phi^*}. \tag{13}$$

So from the knowledge of the system poles and the unscaled mode shapes only, $\boldsymbol{H_a^m}(0)$ can be calculated. Assuming that the mass changes are negligible, $\boldsymbol{H_a^m}(0)$ can be used instead of $\boldsymbol{H}(0)$ for the determination of the stiffness ratio (3), since the mass dependent factor m appears in both the numerator and the denominator.

5. Simulation examples

5.1. Bending stiffness of a simply supported beam with asymmetric damage

A simply supported IPE100 beam of 3 m length is modeled by 64 beam elements having the same length. Suppose that only the vertical displacements at seven equidistant points are measured, and that from these measurements, the receptance matrix $\boldsymbol{H}(\omega)$ between these 7 DOFs can be obtained exactly. Four damage scenario's are considered: (1–3) a stiffness reduction of 5%, 10%, and 20%, respectively between measurement points 2 and 4 and (4) a stiffness reduction of 20% at the eight elements that are adjacent to measurement point 3 (Fig. 6).

At each measurement node, the force configuration of Fig. 5 is used as the $\boldsymbol{f^1}$ configuration and combined with $\boldsymbol{H}(\omega)$ for the undamaged case and $\boldsymbol{H}(\omega) + \Delta\boldsymbol{H}(\omega)$ for the damaged case. The second force configuration $\boldsymbol{f^2}$ corresponding to the 1-norm is chosen. Fig. 7 shows the relative bending stiffness $(EI + \Delta EI)/EI$, estimated using (5), for both damage scenario's.

As can be seen from the figure, the ratio at points 1, 5, 6 and 7 equals exactly 1 since the stress fields induced by the corresponding force configurations are the same in the undamaged and damaged situation. Since for damage scenario 4, nonzero stresses at undamaged locations exist for the virtual force configuration around point 3, the local stiffness

Fig. 6. Damaged simply supported beam: measurement points and *EI* distribution for all four damage scenarios.

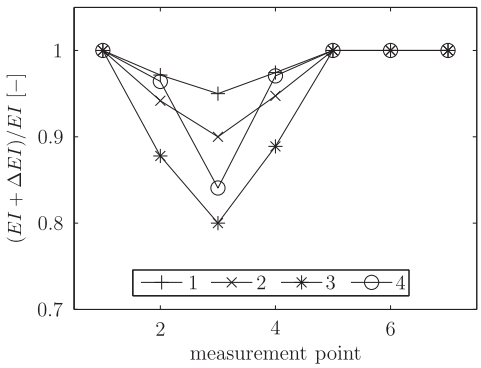

Fig. 7. Damaged simply supported beam: estimated bending stiffness ratio for damage scenario 1 (dashed line) and for damage scenario 2 (full line).

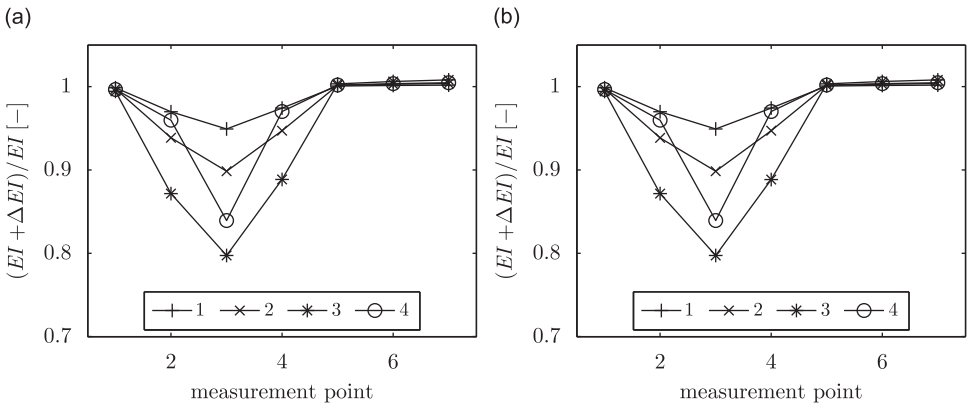

Fig. 8. Damaged simply supported beam: estimated bending stiffness ratio for damage scenario 1 (dashed line) and for damage scenario 2 (full line), estimated using a single mode, (a) obtained from a forced vibration test or (b) obtained from an ambient vibration test.

Fig. 9. Damaged hyperstatic beam: measurement points and *EI* distribution for both damage scenarios.

reduction at this point is slightly underestimated. For damage scenarios 1, 2 and 3, the respective stiffness reductions of 5%, 10% and 20% at node 3 are detected exactly since all nonzero virtual stresses are situated at damaged locations.

If only the first mass-normalized bending mode is used in the construction of $\boldsymbol{H}^{\boldsymbol{m}}(\omega)$ and $\boldsymbol{H}^{\boldsymbol{m}}(\omega)+\Delta\boldsymbol{H}^{\boldsymbol{m}}(\omega)$, i.e. $n=1$ in (7), the damage pattern of Fig. 8a is obtained. The differences with Fig. 7 are negligible. If the first bending mode is not scaled and used for the calculation of $\boldsymbol{H}_{\boldsymbol{a}}^{\boldsymbol{m}}(\omega)$ and $\boldsymbol{H}_{\boldsymbol{a}}^{\boldsymbol{m}}(\omega)+\Delta\boldsymbol{H}_{\boldsymbol{a}}^{\boldsymbol{m}}(\omega)$, the damage pattern of Fig. 8b is obtained. The differences with Figs. 7 and 8a are negligible.

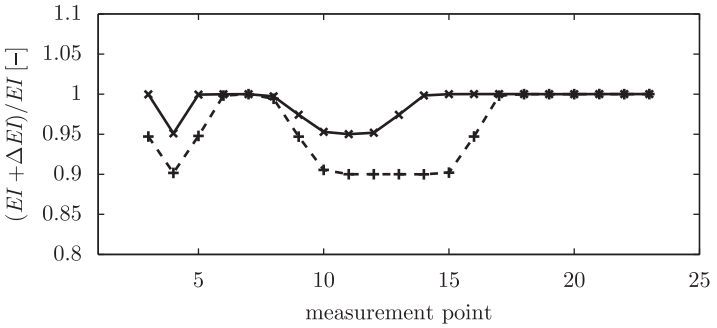

Fig. 10. Damaged hyperstatic beam: estimated bending stiffness ratio for damage scenario 1 (full line) and for damage scenario 2 (dashed line).

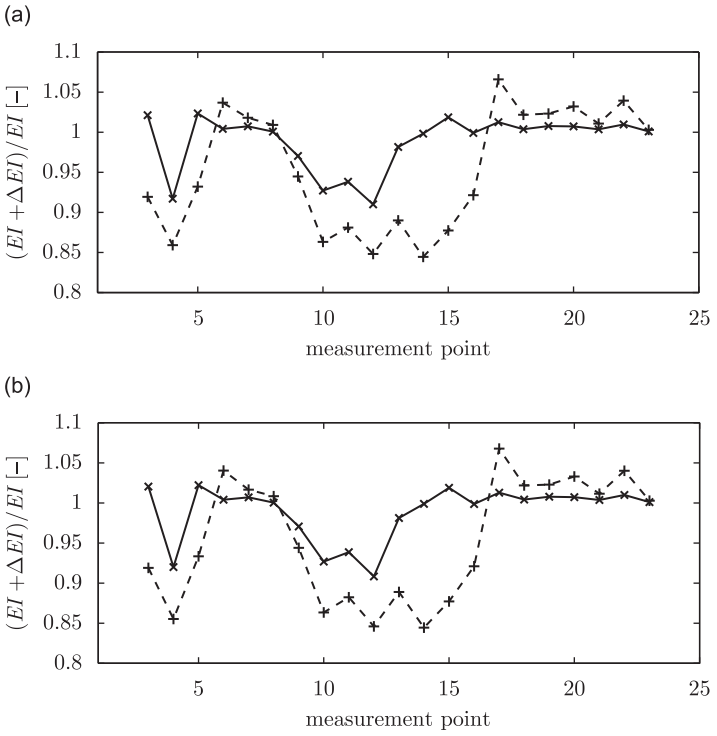

Fig. 11. Damaged hyperstatic beam: estimated bending stiffness ratio for damage scenario 1 (full line) and for damage scenario 2 (dashed line), using the first 12 scaled (a) and unscaled (b) modes.

5.2. *Bending stiffness of a hyperstatic beam with multiple damage locations*

A hyperstatic IPE100 beam of 6 m length is modeled by 48 beam elements of equal length. Suppose that only the vertical displacements at 24 equidistant points are measured, and that from these measurements, the receptance matrix $\boldsymbol{H}(\omega)$ between these 24 DOFs can be obtained exactly. Four damage scenario's are considered (Fig. 9): (1) a stiffness reduction of 5% at the 2 elements that are adjacent to measurement point 4 and between points 9 and 13, (2) a stiffness reduction of 10% between measurement points 3 and 5 and between points 9 and 15, (3) a uniform stiffness reduction of 5% at the shortest span, and (4) an overall stiffness reduction of 5%.

At each measurement node, the force configuration $\boldsymbol{f^1}$ from Fig. 2 is applied and the corresponding displacements at the measured DOFs are calculated using $\boldsymbol{H}(\omega)$ for the undamaged case and $\boldsymbol{H}(\omega)+\Delta\boldsymbol{H}(\omega)$ for the damaged case. It was found that when nonzero stresses exist at both damaged and undamaged locations, the estimated stiffness ratio depends on the choice of the second load configuration $\boldsymbol{f^2}$. After considering several alternatives, the configuration $\boldsymbol{f^2}$ of Fig. 5 was found to yield the best results. Fig. 10 shows the estimated relative bending stiffness $(EI+\Delta EI)/EI$ for the first two damage scenario's, estimated with (4).

As can be seen from the figure, the ratio at points 7 and 15–23 equals exactly 1 for the first damage scenario since the stress fields induced by the corresponding force configurations are the same in the undamaged and damaged situation.

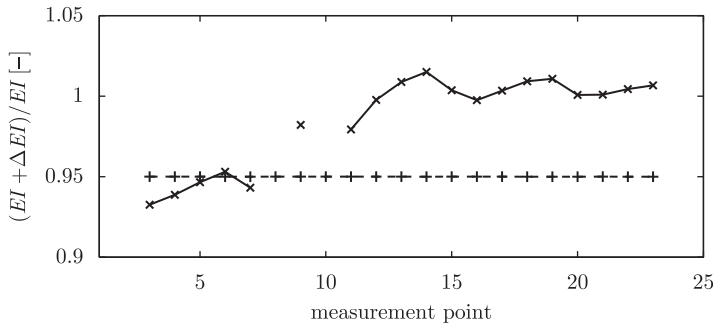

Fig. 12. Damaged hyperstatic beam: estimated bending stiffness ratio for damage scenario 3 (full line) and for damage scenario 4 (dashed line), using the first four unscaled modes and the first unscaled mode, respectively.

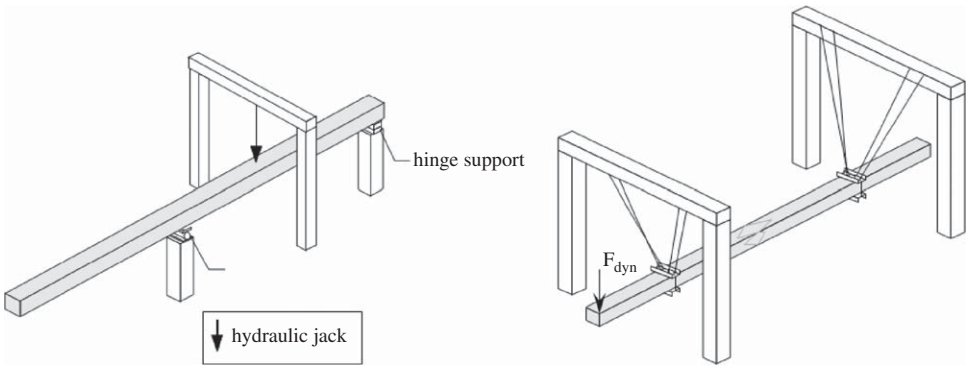

Fig. 13. Reinforced concrete beam: static 3 point bending test setup (left) and dynamic free–free test setup (right).

Similarly, at point 11 the ratio equals exactly 0.95 as predicted by (4). Since nonzero stresses at undamaged locations exist for the force configuration around point 4 (Fig. 2), the local stiffness reduction at this point is underestimated. For the other points, a stiffness ratio between 0.95 and 1 is found since the force configuration around these points induces nonzero stresses at both damaged and undamaged locations.

Similar observations hold for damage scenario 2. It can be noted that the stiffness reduction of 10% at point 4 is detected almost exactly in this case although for this node, nonzero stresses exist at damaged locations.

If only the first 12 scaled modes are used in the construction of $\boldsymbol{H}^{\boldsymbol{m}}(\omega)$ and $\boldsymbol{H}^{\boldsymbol{m}}(\omega)+\Delta\boldsymbol{H}^{\boldsymbol{m}}(\omega)$, i.e. $n=12$ in (7), the damage pattern of Fig. 11(a) is obtained. Although the damage localization is still successful, there is a clear loss of quality in the damage quantification with respect to Fig. 10. This difference increases if less modes are taken into account; it decreases if more modes are taken into account. If unscaled modes are used, i.e. if $\boldsymbol{H}_{\boldsymbol{a}}^{\boldsymbol{m}}(\omega)$ instead of $\boldsymbol{H}^{\boldsymbol{m}}(\omega)$ is used with $n=12$, the results do not change significantly, as can be seen from Fig. 11(b).

The number of modes that need to be taken into account in order to yield accurate damage quantification results was found to depend on the density of the considered measurement grid, the properties of the structure (boundary conditions, stiffness distribution, etc.), and the location, type and extension of the damage. The fact that the number of modes that need to be taken into account depends on the damage type and location is illustrated in Fig. 12, where it is shown that, for damage scenarios 3 and 4, only the first four unscaled modes and the first unscaled mode, respectively, are needed to obtain reasonably good and almost exact results, respectively. This corresponds to the general observation in vibration-based damage identification that the more localized the damage is and the higher the number of separate damaged zones is, the more modes are needed for the identification to be successful. In Section 7, it is shown that, in real-life applications, using the first mode only can already be sufficient, even for hyperstatic structures.

6. Application: damage assessment in a reinforced concrete beam

In this section, the application of the LF method to the damage identification of a reinforced concrete beam of 6 m length that has been gradually damaged using a static three-point bending test, see Fig. 13, is discussed. Between two consecutive loadings, the beam was subject to a free–free vibration test, see Fig. 13. Damage identification on the beam was performed previously using the direct stiffness calculation (DSC) method, a nonparametric damage localization and quantification method that is restricted to beam structures, and using finite element model updating. The results are reported in [14,31],

Table 1
Reinforced concrete beam: load steps.

Load step	Load at 4 m (kN)	Load step	Load at 2 m (kN)
0	0	6	8
1	8	7	10
2	10	8	13
3	13	9	19
4	19	10	25
5	25	11	35
		12	54

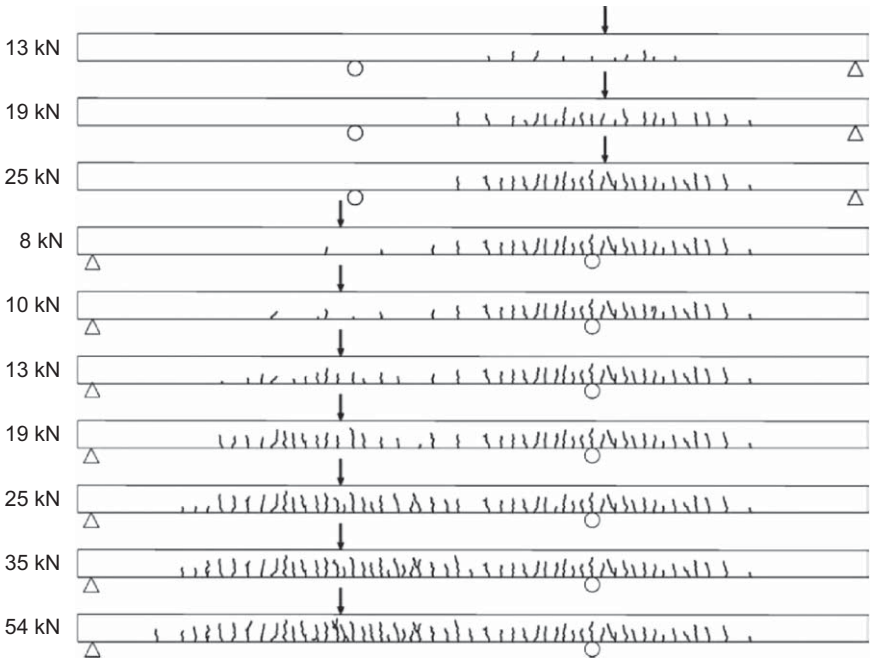

Fig. 14. Reinforced concrete beam: observed cracks (load steps 3–12).

Table 2
Reinforced concrete beam, first three bending modes: measured eigenfrequencies and damping ratios.

Load step	f_1 (Hz)	ξ_1 (%)	f_2 (Hz)	ξ_2 (%)	f_3 (Hz)	ξ_3 (%)
0	22.79	0.9	65.71	0.6	127.35	0.6
1	21.83	1.1	62.79	0.7	122.53	0.7
2	21.53	1.2	61.46	0.9	121.13	0.8
3	21.11	1.3	60.34	1.1	119.79	0.6
4	20.13	1.8	58.14	1.4	115.82	1.0
5	19.43	1.7	57.16	1.4	112.18	1.4
6	19.08	1.8	55.13	1.6	109.92	1.2
7	18.57	2.1	53.01	1.9	107.47	1.4
8	18.21	2.5	51.71	2.3	105.10	2.0
9	18.04	2.0	50.83	2.1	103.92	1.8
10	17.56	1.9	49.48	2.0	101.67	1.7
11	17.31	2.4	49.44	2.1	100.40	1.8
12	17.23	1.6	48.71	1.6	100.77	1.2

respectively. In this section, the damage identification results obtained from the LF method will be compared to the ones obtained from DSC and FEMU.

The load steps for the static loading can be found in Table 1. For load steps 1–5, the load was applied at 4 m from the left end of the beam and the supports where at 2.1 and 5.9 m, respectively. For load steps 6–12, the load was applied at 2 m from the left end with supports at 0.1 and 3.9 m. The first two load steps did not result in visible cracks. Only the last load step resulted in yielding of the reinforcement bars. The observed crack pattern for load steps 3–12 are shown in Fig. 14.

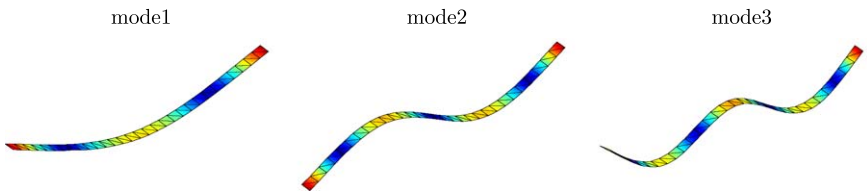

Fig. 15. Reinforced concrete beam: first three bending mode shapes for load step 0.

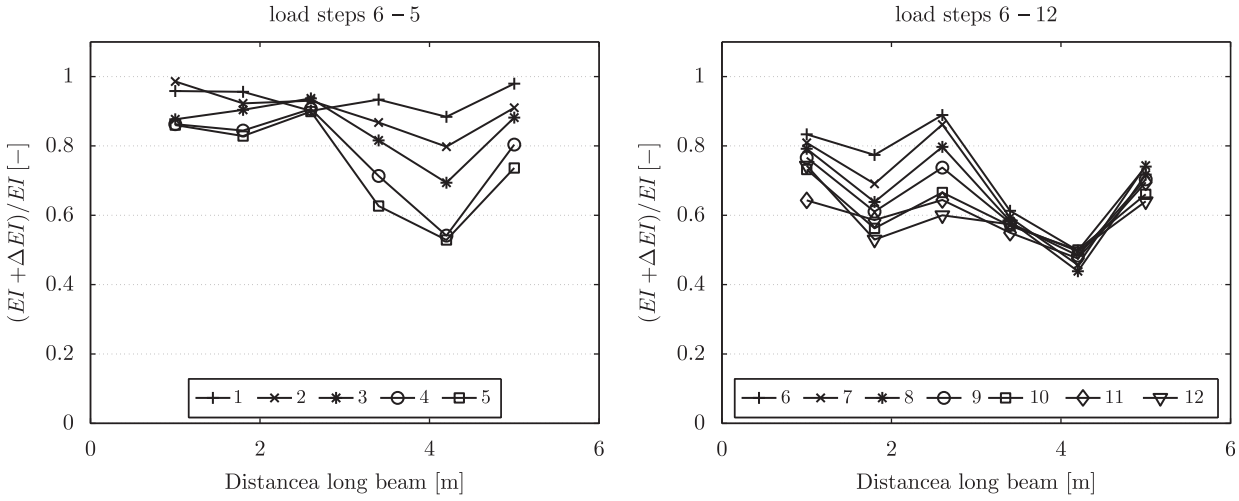

Fig. 16. Reinforced concrete beam: estimated bending stiffness ratio for the different load steps.

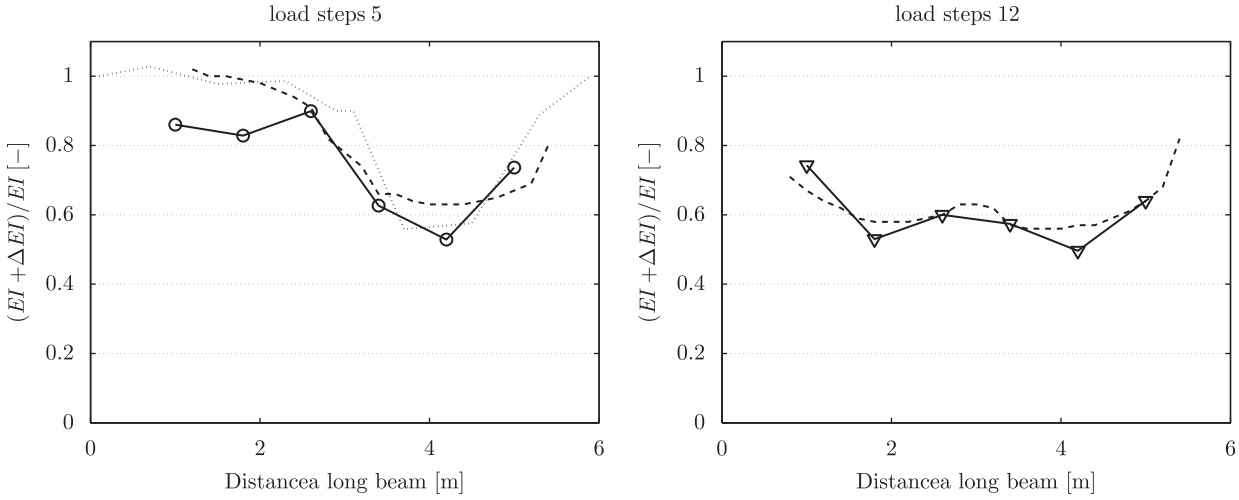

Fig. 17. Comparison of the estimated bending stiffness ratio at load steps 5 and 12 using different damage identification techniques (full line: LF method; dashed line: DSC method; dotted line: FEMU method).

The vibration tests were performed using an impact hammer. The vertical accelerations, resulting from the impact, were measured at intervals of 20 cm in the longitudinal direction of the beam and at both sides in the transversal direction. As a result, 62 DOFs were measured in each vibration test. This was done in six different setups. From the acceleration data only, eigenfrequencies, damping ratios and mode shapes were identified using reference-based data-driven stochastic subspace identification [23], the references being the two reference sensors that were common to the six different setups. The eigenfrequencies and damping ratios for the first three bending modes are shown in Table 2, the mode shapes in Fig. 15.

With the measured ambient modal data, damage identification of the bending stiffness *EI* is performed using (5). Only the first three bending modes are used, since their mode shape estimates are smoother than the ones of the other modes and increasing the number of modes did not improve the results. The modal displacements that were measured at both

sides of the same cross-section are averaged. The virtual load configuration of Fig. 5 can also be used in case of a free–free setup, so it is used here. However, the use of this load configuration in combination with a very dense measurement grid causes numerical problems since differences in adjacent columns of $\boldsymbol{H}_{\boldsymbol{a}}^{\boldsymbol{m}}(0)$ are small in this case, so multiplying with $\boldsymbol{f}_{\boldsymbol{k}}(0)$ results in the subtraction of almost equal quantities. Therefore, only part of the measurement grid is used here. The estimated bending stiffness ratio for the different load steps is shown in Fig. 16. The damage localization and quantification is consistent with the observed crack pattern (Fig. 14).

In Fig. 17, the obtained bending stiffness ratio for load steps 5 and 12 are compared to results obtained with direct stiffness calculation [14], a level 3 nonparametric damage identification method that can be used for beam structures only, and finite element model updating with damage functions [31], which is a parametric method. As for the localization of the damage (level 2 identification), all methods are comparable. As for the quantification, there are differences up to at about 17% bending stiffness change between the methods. This can probably be explained by the fact that they all use different strategies to aggregate the damage over a certain zone of the structure.

7. Application: progressive damage tests on the Z24 bridge

In this section, the application of the LF method to the damage identification of a prestressed concrete bridge that was subjected to a progressive damage test, is discussed. This application is more challenging than the one discussed in the previous section, since it involves a full-scale hyperstatic civil engineering structure. Furthermore, due to the variable cross-section of the bridge, the bending stiffness is not constant, but varies substantially along the length of the bridge girder, even in the undamaged case. As a consequence, the assumption of the LF method that the bending stiffness *EI* is constant in the zones where the virtual stresses are nonzero, is violated also in the undamaged situation. In the simulation examples of Section 5 and the application of Section 6, this was only the case for the damaged situation.

7.1. Structure

The Z24 bridge was a classical post-tensioned concrete two-cell box girder bridge with a main span of 30 m and two side spans of 14 m (Fig. 18). It was part of the road connection between the villages of Koppigen and Utzenstorf, Switzerland, overpassing the A1 highway between Bern and Zürich. The bridge, which dated from 1963, was demolished at the end of 1998, because a new railway adjacent to the highway required a new bridge with a larger side span. Shortly before its demolition, the bridge was subjected to a several progressive damage tests in the framework of the Brite-EuRam project CT96 0277 SIMCES [6]. Before and after each applied damage scenario, the bridge was subjected to a forced and an ambient operational vibration test [26]. Only the ambient tests are considered here.

7.2. Experimental data

With a measurement grid consisting of a regular 3×45 grid on top of the bridge deck and a 2×8 grid on each of the two pillars, a total of 291 degrees of freedom have been measured in nine setups using five reference channels: all acceleration components on the pillars, and mainly vertical and lateral accelerations on the bridge deck. A total of 65 536 samples was collected at a sampling rate of 100 Hz, using an analog anti-aliasing filter with a cutoff frequency of 30 Hz. The data were presented as a benchmark study for algorithms for structural health monitoring and damage identification in the framework of the European Cost Action F3. In the present study, the eigenfrequencies, damping ratios and mode shapes have been extracted from the output-only data using reference-based covariance-driven stochastic subspace identification [23].

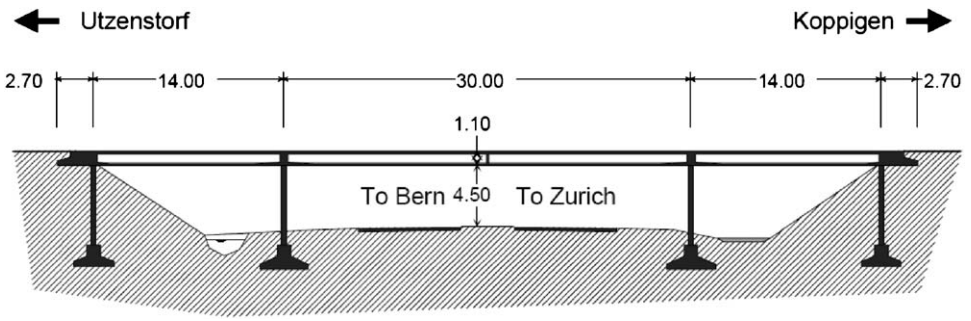

Fig. 18. Side view of the Z24 bridge. Distances are in m.

Table 3
Z24 bridge: overview of progressive damage test scenarios.

No.	Date (1998)	Scenario	Description/simulation of real damage cause
1	04.08	1st reference measurement	Healthy structure
2	09.08	2nd reference measurement	After installation of lowering system
3	10.08	Lowering of pier, 20 mm	Settlement of subsoil, erosion
4	12.08	Lowering of pier, 40 mm	
5	17.08	Lowering of pier, 80 mm	
6	18.08	Lowering of pier, 95 mm	
7	19.08	Tilt of foundation	Settlement of subsoil, erosion
8	20.08	3rd reference measurement	After lifting the bridge to its initial position
9	25.08	Spalling of concrete, 12 m^2	Vehicle impact, carbonization and subsequent corrosion of reinforcement
10	26.08	Spalling of concrete, 24 m^2	
11	27.08	Landslide at abutment	Heavy rainfall, erosion
12	31.08	Failure of concrete hinge	Chloride attack, corrosion
13	02.09	Failure of anchor heads I	Corrosion, overstress
14	03.09	Failure of anchor heads II	
15	07.09	Rupture of tendons I	Erroneous or forgotten injection of tendon tubes, chloride influence
16	08.09	Rupture of tendons II	
17	09.09	Rupture of tendons III	

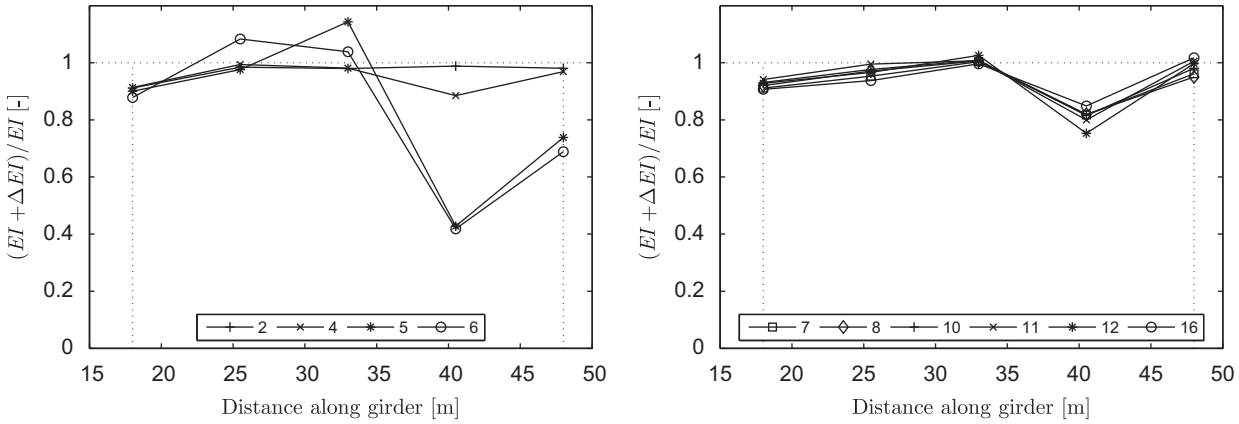

Fig. 19. Z24 bridge: estimated stiffness ratios for different damage scenarios.

7.3. Damage identification

Table 3 provides an overview of the progressive damage tests. From the measured modal data obtained after each scenario, the quasi-static flexibility matrix $\boldsymbol{H}_{\boldsymbol{a}}^{\boldsymbol{m}}(0)$ was calculated using (13). Only the first mode was used in the approximation of the flexibility matrix. Using more modes did not improve the result in this case, probably because the corresponding mode shapes are less smooth than for the first mode. Just as in Section 6, only part of the measured flexibility matrix was used to avoid numerical problems related to the dense measurement grid. Since the bridge deck can be considered as a hyperstatic beam, the load configuration of Fig. 2 was chosen as virtual force configuration. The 1-norm (5) was used for the determination of the stiffness ratios.

Fig. 19 shows the estimated stiffness ratios for different damage scenarios. Scenario 1 was taken as the reference configuration. Due to measurement inaccuracies, the first mode of the third scenario could not be used. The same observations were made in other studies, e.g. [16]. From the figure, the following observations are made.

- The pier settlement of 40 mm (scenario 4) of the Koppigen pier has only a minor influence on the bending stiffness. However, lowering the pier with 80 and 95 mm (scenarios 5 and 6), respectively, has a clear influence on the bending stiffness distribution near this pier. This is explained by the fact that the first cracks in the bridge girder were observed at scenario 5. They were located at the mid span in a zone of 6.6 m from the Koppigen pier. Only one crack was detected at the Koppigen side span, at 1.6 m from the pier. At scenario 6, more cracks appeared at the Koppigen side span, a crack appeared between the girder and the pier, and the other cracks widened somewhat (Fig. 20).
- After the settlement simulation, the pier was raised to its initial position and the cracks closed. As a result, the estimated bending stiffness ratio raised substantially.

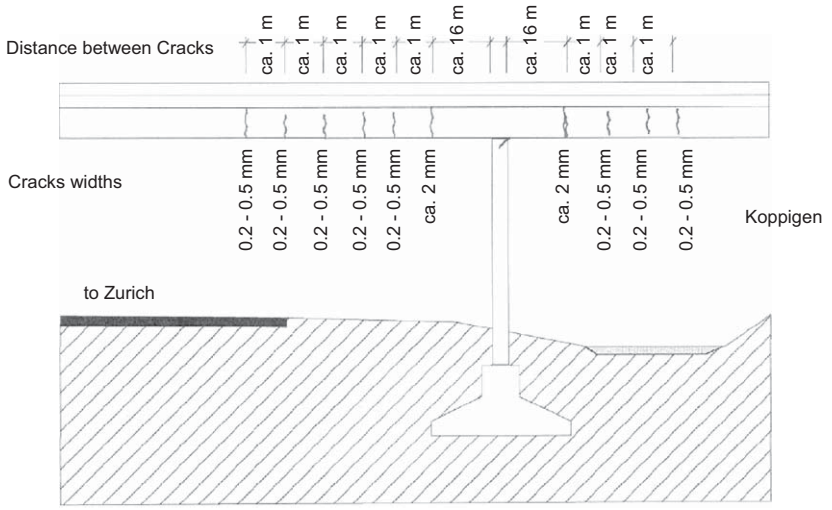

Fig. 20. Z24 bridge: observed cracks after a pier settlement of 90 mm (scenario 6).

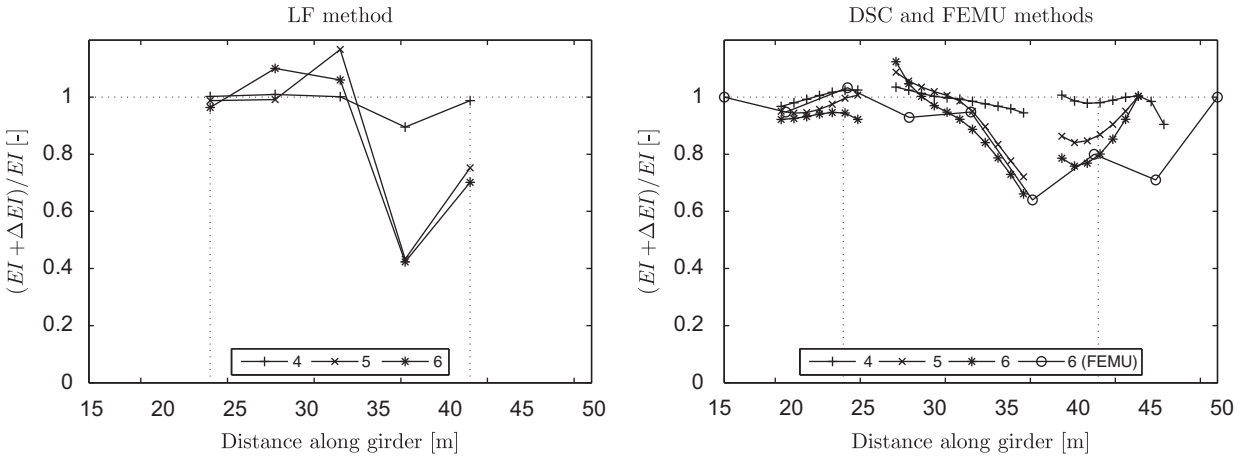

Fig. 21. Z24 bridge: stiffness ratios for different damage scenarios, estimated from the LF, DSC, and FEMU methods.

- All other damage scenarios did not result in further cracks, and the vertical bending stiffness did not change significantly.

These observations are in good qualitative agreement with results presented in the literature [26]. Fig. 21 also provides a quantitative comparison with results obtained with the direct stiffness calculation (DSC) method [16] and the finite element model updating (FEMU) method [32]. Since for both methods, scenario 2 was used as the reference configuration, the same was done for the LF method. All results correspond well, except for the point at 40.5 m along the girder, where there is a pronounced difference between the LF and the other methods, and at 48–55.7 m along the girder (at the Koppigen side span), where there is a pronounced difference between the DSC and the FEMU methods. This can probably be explained by the fact that the three methods use different assumptions and strategies to aggregate the local damage over a certain zone of the structure.

8. Conclusion

A physically rigorous framework was provided for the calculation of a measurable increase in the incremental local flexibility of a critical region of a structure, which can be defined as damage. While the provided framework is in principle valid for any type of structure, the emphasis in this paper was on the estimation of the bending stiffness of beam structures.

Since quasi-static flexibility is directly related to stiffness, environmental influences should be minor or they should cause an overall flexibility change. A decrease in local flexibility with respect to the reference can be directly defined as damage [1].

Simulation examples of damaged isostatic and hyperstatic beams, and experiments involving a reinforced concrete free–free beam and a three-span prestressed concrete bridge, that are both subjected to a progressive damage test, illustrate that:

- If the tested structure is covered by a regular grid of measured DOFs, it is possible to calculate local stiffness changes in adjacent parts of the structure. In this way, a complete set of local stiffness changes can be obtained.
- The estimated local stiffness changes are generally accurate, as evidenced by the comparison with the exact solution in the simulation examples and the comparison with other damage localization and quantification methods in the experiments.
- This accurate estimate can be obtained by measuring only one or a few of the lowest modes of the structure. However, the simulation example with the hyperstatic beam shows that the number of modes needed to obtain accurate results might depend on factors like the location and extent of the damage.
- When mass-normalization of the mode shapes is not possible, for example because they where determined from output-only measurements, but the mass of the structure is approximately equally distributed, the method yields the same results as with mass-normalized mode shapes.
- The parts of the structure, at which one wants to detect a local change in flexibility, cannot be made arbitrarily small due to numerical reasons, since for very small zones combining the quasi-static flexibility with the virtual load configuration $\boldsymbol{f}^{\mathbf{1}}$ could cause the loss of several digits of accuracy.
- If the structure's mass is approximately equally distributed and if a lumped mass assumption is valid, it is possible to get an accurate estimate of the quasi-static flexibility using output-only vibration measurements up to a mass dependent scalar, without estimating the analytical mass matrix.

When applied with care, the local flexibility method presented in this paper can be a valuable method for non-model-based damage detection, localization and quantification. It generates local stiffness distributions that could be used directly or as starting values for model-based damage identification methods such as finite element model updating techniques.

References

[1] A.E. Aktan, K.L. Lee, C. Chuntavan, T. Aksel, Modal testing for structural identification and condition assessment of constructed facilities, *Proceedings of 12th International Modal Analysis Conference*, Honolulu, HI, 1994, pp. 462–468.
[2] J.V. Araújo dos Santos, C.M. Mota Soares, C.A. Mota Soares, N.M.M. Maia, Structural damage identification in laminated structures using FRF data, *Composite Structures* 67 (2005) 239–249.
[3] D. Bernal, Extracting flexibility matrices from state-space realizations, *European COST F3 Conference*, Madrid, Spain, 2000, pp. 127–135.
[4] D. Bernal, Load vectors for damage localization, *ASCE Journal of Engineering Mechanics* 128 (1) (2002) 7–14.
[5] D. Bernal, The stochastic dynamic damage locating vector approach, *Proceedings of the 25th International Modal Analysis Conference*, Orlando, FL, 2007.
[6] G. De Roeck, The state-of-the-art of damage detection by vibration monitoring: the SIMCES experience, *Journal of Structural Control* 10 (2003) 127–143.
[7] S.W. Doebling, C.R. Farrar, M.B. Prime, D.W. Shevitz, Damage identification and health monitoring of structural and mechanical systems from changes in their vibration characteristics: a literature review, Report LA-13070-MS, Los Alamos National Laboratory, Los Alamos, NM, 1996.
[8] D.J. Ewins, *Modal Testing*, second ed., Research Studies Press, Baldock, UK, 2000.
[9] C.H.J. Fox, The location of defects in structures: a comparison of the use of natural frequency and mode shape data, *Proceedings of the IMAC X conference*, San Diego, CA, 1992, pp. 522–528.
[10] W. Heylen, S. Lammens, P. Sas, *Modal Analysis Theory and Testing*, Department of Mechanical Engineering, Katholieke Universiteit Leuven, Leuven, Belgium, 1997.
[11] J. Holland, *Adaptation in Natural and Artificial Systems*, University of Michigan Press, Ann Arbor, MI, 1975.
[12] J.-N. Juang, *Applied System Identification*, Prentice-Hall, Englewood Cliffs, NJ, 1994.
[13] S. Kirkpatrick, C.D. Gelatt, M.P. Vecchi, Optimization by simulated annealing, *Science* 220 (1983) 671–680.
[14] J. Maeck, Damage Assessment of Civil Engineering Structures by Vibration Monitoring, PhD Thesis, Department of Civil Engineering, K.U. Leuven, 2003.
[15] J. Maeck, G. De Roeck, Dynamic bending and torsion stiffness derivation from modal curvatures and torsion rates, *Journal of Sound and Vibration* 225 (1) (1999) 153–170.
[16] J. Maeck, B. Peeters, G. De Roeck, Damage identification on the Z24-bridge using vibration monitoring analysis, *Smart Materials and Structures* 10 (3) (2001) 512–517.
[17] N.M.M. Maia, J.M.M. Silva, *Theoretical and Experimental Modal Analysis*, Research Studies Press, Taunton, UK, 1997.
[18] R.L. Mayes, An experimental algorithm for detecting damage applied to the i-40 bridge over the Rio Grande, *Proceedings of the 13th International Modal Analysis Conference*, Nashville, TN, February 13–16, 1995, pp. 219–225.
[19] J.E. Mottershead, M.I. Friswell, Model updating in structural dynamics: a survey, *Journal of Sound and Vibration* 167 (2) (1993) 347–375.
[20] A.K. Pandey, M. Biswas, Damage detection in structures using changes in flexibility, *Journal of Sound and Vibration* 169 (1) (1994) 3–17.
[21] A.K. Pandey, M. Biswas, Experimental verification of flexibility difference method for locating damage in structures, *Journal of Sound and Vibration* 184 (2) (1995) 311–328.
[22] A.K. Pandey, M. Biswas, M.M. Samman, Damage detection from changes in curvature mode shapes, *Journal of Sound and Vibration* 145 (2) (1991) 321–332.
[23] B. Peeters, G. De Roeck, Reference-based stochastic subspace identification for output-only modal analysis, *Mechanical Systems and Signal Processing* 13 (6) (1999) 855–878.
[24] B. Peeters, G. De Roeck, One-year monitoring of the Z24-bridge: environmental effects versus damage events, *Earthquake Engineering and Structural Dynamics* 30 (2001) 149–171.
[25] B. Peeters, J. Maeck, G. De Roeck, Vibration-based damage detection in civil engineering: excitation sources and temperature effects, *Smart Materials and Structures* 10 (3) (2001) 518–527.
[26] E. Reynders, G. De Roeck, Continuous vibration monitoring and progressive damage testing on the Z24 bridge, in: C. Boller, F.K. Chang, Y. Fujino (Eds.), *Encyclopedia of Structural Health Monitoring*, Wiley, New York, 2009, pp. 2149–2158.

[27] E. Reynders, G. De Roeck, P.G. Bakir, C. Sauvage, Damage identification on the Tilff bridge by vibration monitoring using optical fibre strain sensors, *ASCE Journal of Engineering Mechanics* 133 (2) (2007) 185–193.
[28] A. Rytter, Vibration Based Inspection of Civil Engineering Structures, PhD Thesis, Aalborg University, 1993.
[29] O.S. Salawu, Nondestructive assessment of structures using the integrity index method applied to a concrete highway bridge, *Insight* 37 (11) (1995) 875–878.
[30] H. Sohn, C.R. Farrar, F.M. Hemez, D.D. Shunk, D.W. Stinemates, B.R. Nadler, A review of structural health monitoring literature: 1996–2001, Report LA-13976-MS, Los Alamos National Laboratory, Los Alamos, NM, 2003.
[31] A. Teughels, Inverse Modelling of Civil Engineering Structures Based on Operational Modal Data, PhD Thesis, Department of Civil Engineering, K.U.Leuven, 2003.
[32] A. Teughels, G. De Roeck, Structural damage identification of the highway bridge Z24 by FE model updating, *Journal of Sound and Vibration* 278 (3) (2004) 589–610.
[33] A. Teughels, G. De Roeck, J.A.K. Suykens, Global optimization by coupled local minimizers and its application to FE model updating, *Computers and Structures* 81 (24–25) (2003) 2337–2351.
[34] T. Toksoy, A.E. Aktan, Bridge-condition assessment by modal flexibility, *Experimental Mechanics* 34 (3) (1994) 271–278.
[35] D.K. Watson, R.K.N.D. Rajapakse, Seasonal variation in material properties of a flexible pavement, *Canadian Journal of Civil Engineering* 27 (1) (2000) 44–54.
[36] W.M. West, Illustration of the use of modal assurance criterion to detect structural changes in an orbiter test specimen, *Proceedings of the Air Force Conference on Aircraft Structural Integrity*, 1984, pp. 1–6.
[37] M.M.F. Yuen, A numerical study of the eigenparameters of a damaged cantilever, *Journal of Sound and Vibration* 103 (3) (1985) 301–310.
[38] Z. Zhang, A.E. Aktan, The damage indices for the constructed facilities, *Proceedings of the 13th International Modal Analysis Conference*, Nashville, TN, February 13–16, 1995, pp. 1520–1529.